

## TEM Investigation of the Microstructure of the Scale Formed on a FeCrAlRE Alloy at 900 °C: The Effect of Y-rich RE Particles

Fang Liu · Helena Götlind · Jan-Erik Svensson ·  
Lars-Gunnar Johansson · Mats Halvarsson

Received: 10 July 2009/Revised: 14 January 2010/Published online: 24 March 2010  
© Springer Science+Business Media, LLC 2010

**Abstract** Three oxide features: the thin and smooth protective oxide, reactive element (Ti-, Zr- or Y-rich) particles, and patches of thick oxide surrounding the Y-rich reactive element particles, were observed on a commercial FeCrAlRE alloy, Kanthal AF, exposed at 900 °C. The microstructural development of the patches of thick oxide was investigated on samples exposed for 24 or 168 h in either dry O<sub>2</sub> or O<sub>2</sub> + 40% H<sub>2</sub>O. Analytical transmission electron microscopy in combination with site-precision TEM sample preparation by FIB/SEM was used. In all patches a thin but continuous inward growing  $\alpha$ -Al<sub>2</sub>O<sub>3</sub> layer was formed under a thick outward growing alumina layer, which initially consisted only of  $\gamma$ -Al<sub>2</sub>O<sub>3</sub>. In dry O<sub>2</sub>, transformation of  $\gamma$ -Al<sub>2</sub>O<sub>3</sub> (in the outer layer) to  $\alpha$ -Al<sub>2</sub>O<sub>3</sub> had started during 24 h and a considerable amount of  $\gamma$ -Al<sub>2</sub>O<sub>3</sub> had transformed after 168 h. The transformation originated immediately above the inward growing  $\alpha$ -Al<sub>2</sub>O<sub>3</sub>. No such transformation occurred in O<sub>2</sub> + H<sub>2</sub>O. The possible effects of the Y-rich RE particles, as well as the effects of water vapour, on the oxidation were discussed.

**Keywords** FeCrAl alloy · RE · Y · Al<sub>2</sub>O<sub>3</sub> · Microstructure · FIB/SEM · TEM · EDX · High temperature oxidation · Water vapour · Phase transformation

---

F. Liu (✉) · M. Halvarsson  
Department of Applied Physics, Chalmers University of Technology, 41296 Göteborg, Sweden  
e-mail: fang.liu@chalmers.se

H. Götlind · J.-E. Svensson · L.-G. Johansson  
Department of Chemical and Biological Engineering, Chalmers University of Technology,  
41296 Göteborg, Sweden

L.-G. Johansson  
Swedish High Temperature Corrosion Centre,  
41296 Göteborg, Sweden

## Introduction

FeCrAl alloys have excellent oxidation resistance at elevated temperatures and are therefore widely used as high temperature materials. Their good high temperature corrosion properties rely on the formation of a dense and well-adherent  $\alpha$ -Al<sub>2</sub>O<sub>3</sub> scale. Issues of great concern are (among others): the adherence of  $\alpha$ -Al<sub>2</sub>O<sub>3</sub> [1] and the possible formation of metastable aluminas, especially at temperatures below 950 °C [2].

$\alpha$ -Al<sub>2</sub>O<sub>3</sub> scales are often susceptible to spallation and mechanical failure induced by various factors, such as growth stresses, thermal stresses, and stresses applied in service. It is well established that small additions of reactive elements (REs), commonly Y, Zr, Hf and La, to FeCrAl alloys can greatly decrease the tendency for oxide spallation, and thus improve the oxidation behaviour of these alloys [3]. The beneficial effect of RE additions has been subjected to extensive study for more than 30 years, and many theories have been proposed in order to explain the mechanisms behind it [3]. The most widely recognized explanations are:

- The addition of REs modifies the oxide scale growth mechanism to dominant inward oxygen diffusion [4–6].
- REs improve oxide adherence by gettering sulphur in the alloy [7–11]. Sulphur can segregate at the alloy/oxide interface, thus weakening the adhesion of the oxide scale to the alloy [12, 13].
- The formation of RE containing “oxide pegs” in the scale provides mechanical keying to the substrate alloy [14–16].
- REs may enhance interfacial chemical bonding [17–20].

It has been reported that the concentration of RE in the alloy plays a very important role for oxidation resistance. Thus, Klöwer observed that when the Y concentration was above a certain level, substantial internal oxidation led to a rapid wastage of material and thus a strong reduction of the lifetime of these alloys [21]. This effect was termed “overdoping”. As might be expected, the effect on oxidation behaviour depends on the specific RE elements added [22–24]. For example, Wessel et al. reports that the oxide morphology changes from columnar in a Y-containing version of a FeCrAl alloy to small equiaxed grains in a (Zr + Y)-containing version of the same material [24]. The reasons behind these differences are not known.

Under certain circumstances, for instance at low temperature or short exposure times, metastable transient aluminas, e.g.  $\gamma$ -Al<sub>2</sub>O<sub>3</sub> and  $\theta$ -Al<sub>2</sub>O<sub>3</sub>, are formed instead of the thermodynamically stable phase  $\alpha$ -Al<sub>2</sub>O<sub>3</sub>. If the temperature is high enough, the transient aluminas transform with time, forming  $\alpha$ -Al<sub>2</sub>O<sub>3</sub>. A series of recent studies have shown that the transformation is influenced by the gas composition—whether water vapour is present or not [25–29]. In those studies a commercial FeCrAlRE alloy, Kanthal AF, was oxidized at 900 °C in dry O<sub>2</sub> or O<sub>2</sub> + 40% H<sub>2</sub>O for different periods of time. Three oxide features were observed: thin and smooth “base” oxide, RE particles, and thick oxide patches surrounding the Y-rich RE particles. Detailed microstructure investigations of the base oxide by Transmission Electron Microscopy (TEM) were carried out, and an oxidation mechanism including the influence of water vapour was proposed [25, 27, 29]. A preceding

paper reported on the effect of different RE particles, Y-, Zr- or Ti-rich [26], on oxidized Kanthal AF samples. It revealed that only Y-rich RE particles were found at the centre of thick oxide patches, while the Zr- or Ti-rich RE particles were surrounded by a thin and smooth oxide scale. Very few reports in the literature deal with this specific aspect of Y additions: i.e. that Y-rich RE particles locally enhance the growth of the oxide scale.

The present study contains a detailed microstructural investigation of the oxide scales formed around Y-rich RE particles on the surface of a FeCrAlRE alloy (Kanthal AF) at 900 °C. Comparisons are made between scales formed after 24 and 168 h in dry O<sub>2</sub> and in O<sub>2</sub> + H<sub>2</sub>O. The aim is to shed more light on the influence of the Y-rich particles on the growth of the neighbouring scale and to elucidate further the effect of water vapour on the oxidation mechanism. For this purpose analytical TEM was employed to examine cross-section specimens containing the interesting features, i.e. the Y-rich RE particles and the surrounding oxide scale regions.

## Experimental

### Exposure

Table 1 gives the nominal chemical composition of the material used in this study, Kanthal AF. The alloy had a typical grain size in the range 10–20 μm. The SEM (secondary electron) image and SEM/EDX maps in Fig. 1 show several RE-rich

**Table 1** Chemical composition of Kanthal AF

Element	Fe	Cr	Al	Ti	Y	Zr	Mg	Si	C
Wt. %	Bal.	21.3	5.1	0.08	0.03	0.06	0.001	0.3	0.03

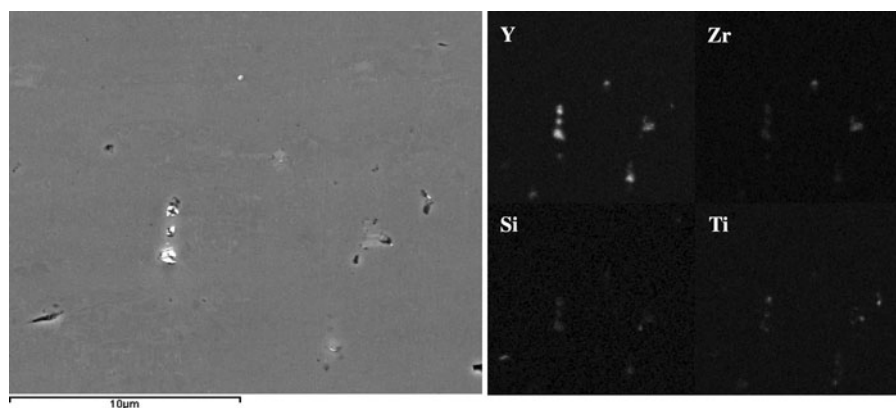


**Fig. 1** SEM secondary electron image and SEM/EDX maps of RE-rich particles on an unexposed sample

particles with complex chemical compositions in the un-exposed material. The particle size is around 1–2 micrometers and they tend to be located at the alloy grain boundaries. Most particles contain a mixture of Y, Zr and Ti (although some are Y-rich, some are Zr-rich and some are Ti-rich), and some of them contain Si. A few Y-rich particles also contain some O, however no YAG was found. Coupons (15 mm × 15 mm × 2 mm) were ground and fine polished down to 1 μm diamond finish, cleaned in ethanol using ultrasonic agitation, and then rinsed in acetone and ethanol before exposure. Samples were exposed in a horizontal tube furnace at  $900 \pm 3$  °C for 24 and 168 h in either dry O<sub>2</sub> (referred to as the dry environment) or O<sub>2</sub> with 40 vol.% H<sub>2</sub>O (referred to as the humid environment) with a gas flow velocity of 4 cm/s. The water vapour concentration in the dry O<sub>2</sub> exposures is about 5 ppm. A detailed description of the furnace set-up can be found in previous papers [28, 30].

### SEM and TEM Analysis

The oxidized samples were first analysed by scanning electron microscopy (SEM) and Energy Dispersive X-ray analysis (EDX). In order to prepare TEM windows with oxide features of interest the in situ lift-out technique was employed in an FEI Strata DB 235 workstation, a combined Focused Ion Beam Microscope/Scanning Electron Microscope (FIB/SEM), equipped with an Omniprobe micromanipulator. The SEM part was used to choose areas for the TEM windows and to acquire secondary electron images. In order to protect the oxide scale, a layer of Pt was deposited with the aid of the gas injection system in the workstation. A detailed description of this sample preparation process technique was reported elsewhere [31]. A Philips CM 200 FEG TEM, equipped with an EDX system was used. The TEM was operated at 200 kV. The TEM windows were also analyzed by a Leo Ultra 55 FEG SEM equipped with an Oxford Inca EDX system. The SEM was operated at different voltages for different purposes: at 30 kV for analysis of the TEM windows, at 10 kV for imaging the bulk oxidized sample with backscattered electrons and 20 kV for SEM/EDX. The quantitative results (EDX spot analyses and linescans) presented in this study show element concentrations as a weight or atomic percentage of the total cation content, i.e. all cations present add up to 100 wt.% or at.%.

## Results

### General Oxide Features

Figure 2 is an overview SEM backscattered electron image after 24 h exposure to dry O<sub>2</sub>. Three characteristic morphologies can be seen; the thin base oxide, RE-rich particles and patches of thick oxide. These general features were present on all samples regardless of exposure time and environment. The base oxide (the grey regions) covers most of the sample surface, and detailed investigations of it have been reported elsewhere [27, 29]. Because of the higher average atomic number the

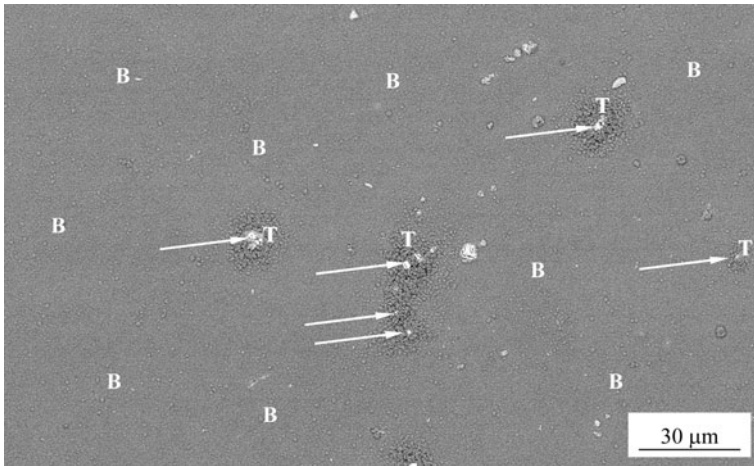


**Fig. 2** Surface morphology of the oxide scale formed on Kanthal AF at 900 °C as imaged in the SEM using backscattered electrons. There are three main oxide features: the base oxide (labeled “B”) that covers most of the surface, the bright RE particles, and the thick oxide patches (labeled “T”) that surround only the Y-rich RE particles (*arrowed*). The sample was exposed in O<sub>2</sub> for 24 h

RE-enriched particles appear bright in the backscattered electron image. EDX analysis revealed that some of the RE rich particles are rich in Y, while others are rich in Zr or Ti. Interestingly, the third feature, the patches of thick oxide, always form around the Y-rich RE particles (*arrowed* in Fig. 2), while the Zr- or Ti-rich particles are surrounded by base oxide. A preliminary study of this phenomenon was published earlier [26]. In the present paper the development of the Y-rich RE particles and the surrounding patches of thick oxide will be examined in more detail.

### SEM Overview of Y-Rich RE Particles and the Surrounding Oxide Scale Regions

A closer look at the areas with Y-rich RE particles allows a comparison of the detailed morphology. The SEM secondary electron images in Fig. 3 show the samples after 24 and 168 h exposure in dry and wet O<sub>2</sub>. The two time-resolved series, Fig. 3a, c; and b, d, in wet and dry O<sub>2</sub>, respectively, illustrate how the patches of thick oxide surrounding the Y-rich RE particles grow thicker and merge. An inspection of Fig. 3 also shows that the presence of water vapour affects the morphology of the patches of thick oxide. In wet O<sub>2</sub>, the oxide grains are closely packed, forming a rather smooth surface, while in the dry O<sub>2</sub> the oxide grains protrude from the surface, forming a rough, blade-like morphology. To further elucidate the microstructure of the Y-rich RE particles and the surrounding patches of thick oxide, the *in situ* lift-out technique in the FIB/SEM was used to prepare site-precision cross-section TEM samples. Note that the TEM windows shown in the following subsections were lifted out from the exact areas shown in Fig. 3. The dashed-lines show approximately where the TEM windows were located.

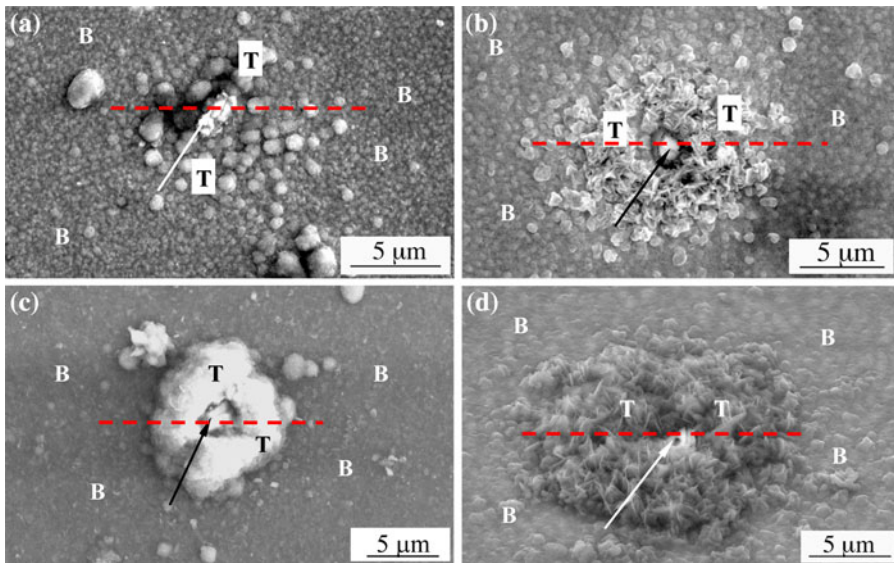


**Fig. 3** Plan view images of Y-rich RE particles (*arrowed*) and the surrounding oxide scale (the thick oxide patches (labeled “T”) and the base oxide (labeled “B”)) on samples exposed at 900 °C. **a** 24 h in O<sub>2</sub> with H<sub>2</sub>O. **b** 24 h in dry O<sub>2</sub>. **c** 168 h in O<sub>2</sub> with H<sub>2</sub>O. **d** 168 h in dry O<sub>2</sub> (*slightly tilted*). Note that these are the exact areas from which the crosssection lift-out TEM samples were taken. The *dashed-lines* show approximately where the TEM windows located originally on the sample (FIB/SEM secondary electron image)

The results acquired by analytical TEM from these samples are presented in the following sections.

#### TEM Investigation After 24 h in O<sub>2</sub> + 40% H<sub>2</sub>O

The TEM bright field image in Fig. 4a displays an overview of the cross-section TEM window from a sample exposed for 24 h in wet O<sub>2</sub>. The Y-rich RE particle has a diameter of  $\sim 2 \mu\text{m}$  and is embedded  $\sim 1 \mu\text{m}$  into the alloy. Adjacent to the particle (on both sides) the oxide scale is thick. At a distance from the particle, the thin base oxide is present. Overall, the gas/oxide interface is rather smooth, which is consistent with the SEM imaging, see Fig. 3a. Figure 4b showing an enlarged image of the rectangular boxed area indicated in Fig. 4a reveals that the oxide is layered. There is a relatively thin but continuous inner layer made up of equiaxed grains and a thicker outer layer containing columnar grains. The grains in the outer layer feature a large number of dark straight lines, indicating the presence of defects. This morphology is characteristic of  $\gamma\text{-Al}_2\text{O}_3$  [32, 33]. The identification of  $\gamma\text{-Al}_2\text{O}_3$  in the outer layer of the scale was verified by electron diffraction as shown in Fig. 6. The boundary between the two layers is highlighted by the dashed line in Fig. 4b. The total oxide thickness is about 800 nm with the inner layer being around 100 nm. A number of voids can be seen close to the interface between the inner and outer layer. In addition, there are voids in the outer layer.

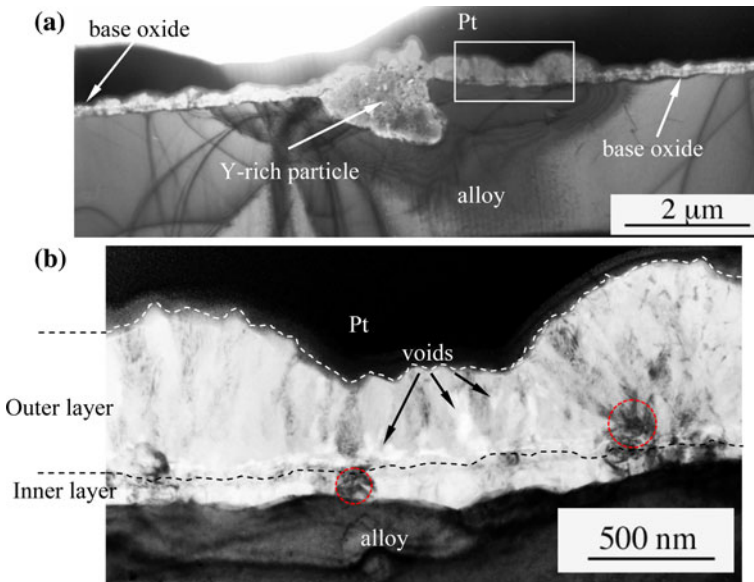


**Fig. 4** **a** TEM bright field cross-section image of the oxide scale formed on the sample exposed to  $O_2$  with 40%  $H_2O$  for 24 h (See Fig. 3a). The oxide scale close to the Y-rich particle is much thicker than the base oxide. **b** Enlarged image of the boxed area in (a), showing a two-layered structure. The top Pt-layer was deposited during the TEM window preparation in the FIB/SEM. Diffraction patterns of the circled grains are presented in Fig. 6a, b

STEM/EDX maps were acquired centred on the Y-rich particle. The O, Al, Y, Zr and Ti maps are shown in Fig. 5 together with the STEM bright field image. The particle contains mainly Y with some Zr and Ti. The composition of the particle varies. A typical composition for the Y-rich part is (out of cations): Y 55 at.%, Zr 10 at.%, Ti <5 at.%, the balance being mainly Fe, Cr and Al. A 200 nm thick alumina layer separates the particle entirely from the underlying alloy. There is also some alumina on top of the particle.

TEM convergent beam electron diffraction (CBED) was used to identify the crystal structure of the alumina grains in Fig. 4. Several CBED patterns were acquired from the two-layered thick oxide as well as from the scale underneath the Y-rich particle. The results show that the outer layer of the thick oxide patch consists of  $\gamma$ - $Al_2O_3$  while the inner layer is made up of  $\alpha$ - $Al_2O_3$ . The oxide scale below the particle also consists of  $\alpha$ - $Al_2O_3$ . Typical CBED patterns from different positions, those circled in Figs. 4b and 5, are shown, respectively in Fig. 6a–c. The positions of the oxide grains are. The zone axes are [001],  $[1\bar{1}00]$  and  $[\bar{2}20\bar{1}]$ , respectively.

#### TEM Investigation after 24 h in Dry $O_2$

Figure 7a shows a TEM bright field cross-section image of a patch of thick oxide surrounding an Y-rich particle after 24 h in dry  $O_2$ . The rather rough surface

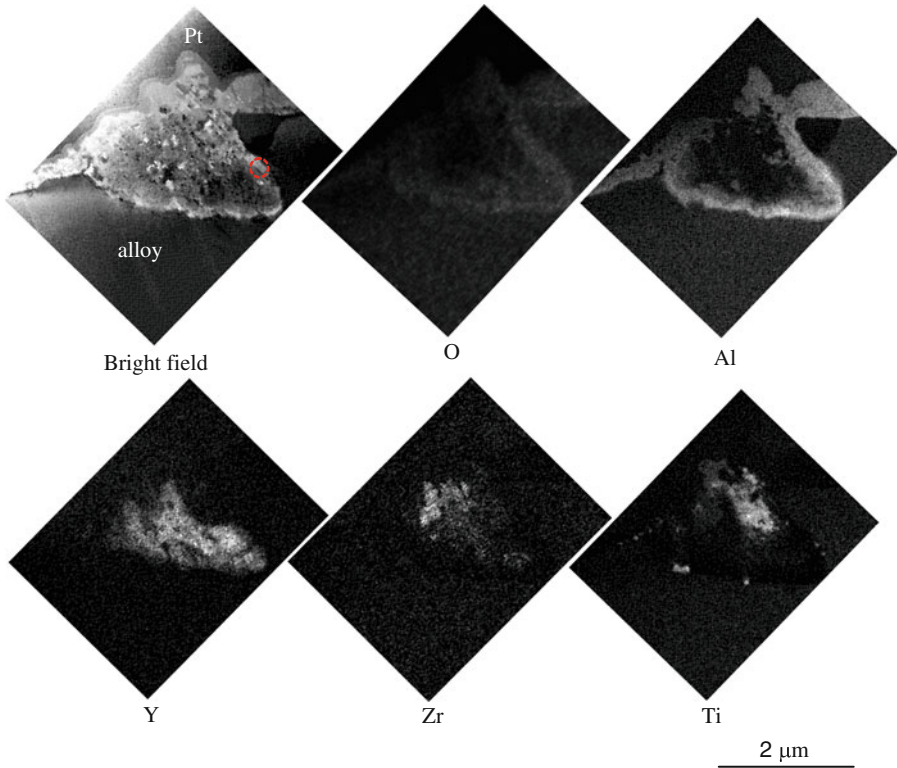


**Fig. 5** STEM bright field image and STEM/EDX maps of the Y-rich RE particle (24 h, O<sub>2</sub> with 40% H<sub>2</sub>O). The particle is oxidized and contains some Zr and Ti in addition to Y. A continuous alumina layer separates the particle from the alloy substrate. Diffraction pattern of the circled grain is presented in Fig. 6c

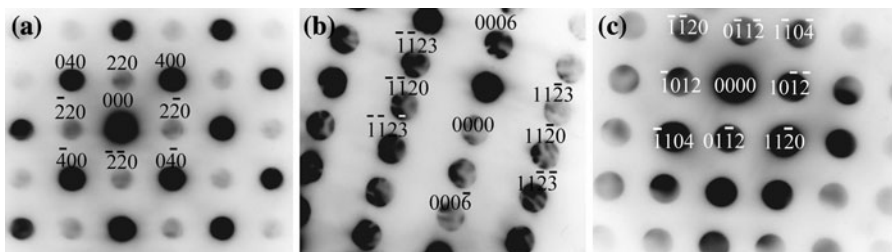


**Fig. 6** CBED patterns from circled oxide grains in Figs. 4 and 5 (24 h, O<sub>2</sub> with 40% H<sub>2</sub>O). **a** Diffraction pattern from a grain in the outer layer, indexed as  $\gamma$ -Al<sub>2</sub>O<sub>3</sub>, with zone axis [001]. **b** Pattern from a grain in the inner layer, indexed as  $\alpha$ -Al<sub>2</sub>O<sub>3</sub>, with zone axis [110]. **c** A pattern from a grain in the oxide layer underneath the RE particle indexed as  $\alpha$ -Al<sub>2</sub>O<sub>3</sub>, with zone axis [220]

morphology corresponds to the blade-like morphology observed by SEM (Fig. 3b). The TEM image reveals that the oxide scale is close to 1  $\mu\text{m}$  thick, with the tips of the blades sticking out 100–300 nm. Although it is hard to tell from the micrograph,



the oxide scale consists of two layers as in the corresponding exposure in humid environment. The oxide grains in the outer layer are elongated and contain a large number of planar defects, typical for  $\gamma$ - $\text{Al}_2\text{O}_3$ . In some locations, defect-free equiaxed oxide grains (larger than 100 nm) were observed at the bottom of the outer layer. The inner layer is very thin, with oxide grains  $\sim 40$  nm in size. Similar to the corresponding exposures in humid environment, there are voids close to the interface between the oxide layers as well as in the outer oxide. Figure 7b shows a STEM/EDX linescan (the position of which is indicated in Fig. 7a as the line AB) across the oxide scale. The linescan shows that the oxide scale can be divided into three regions, according to the chemical composition. At the bottom of the oxide there is a very thin Al-rich region (I) which is covered by a Cr-rich region (II). The top part is thick and dominated by Al (III). The scale structure is similar to that in the corresponding humid exposure. Electron diffraction also showed a similar phase composition as in the corresponding humid exposure, the outer layer consisting mainly of  $\gamma$ - $\text{Al}_2\text{O}_3$ , and the inner layer consisting of  $\alpha$ - $\text{Al}_2\text{O}_3$ . The main difference was the  $\sim 100$  nm large equiaxed defect-free grains located immediately above the

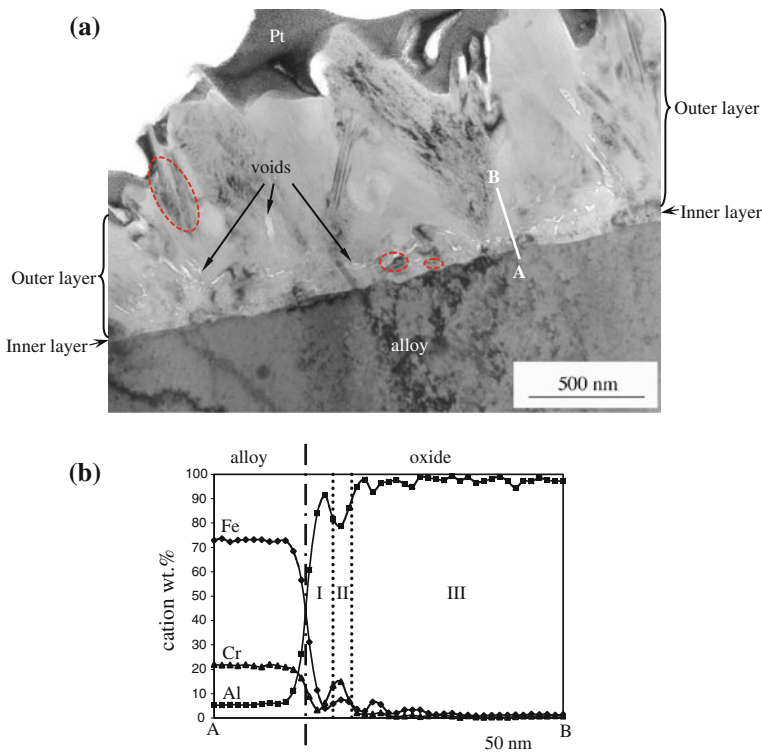


**Fig. 7** **a** TEM bright field cross-section image of a thick oxide patch close to an Y-rich particle on the sample exposed to  $\text{O}_2$  for 24 h (See Fig. 3b). The line AB indicates the position where the linescan was acquired. Diffraction patterns of the circled grains are presented in Fig. 8. **b** STEM/EDX linescan across the thick oxide patch. The variations in the Al and Cr EDX linescan profiles shows that the oxide is layered with I = the inner layer, II = the Cr rich band, III = the outer layer

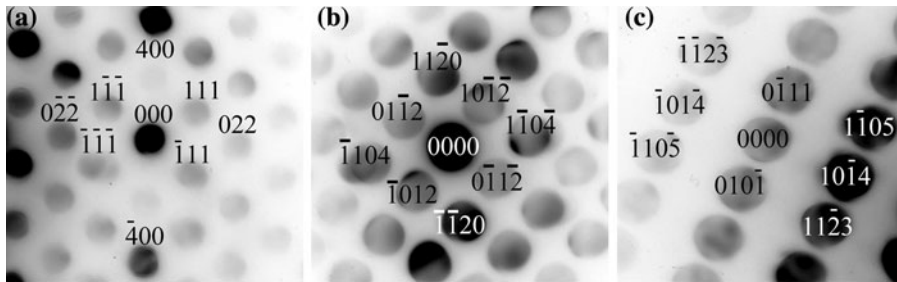


**Fig. 8** CBED patterns from *circled* oxide grains in the thick oxide patch in Fig. 7 (24 h, O<sub>2</sub>). **a** Diffraction pattern from a grain in the outer layer, indexed as  $\gamma$ -Al<sub>2</sub>O<sub>3</sub>, with zone axis [01 $\bar{1}$ ]. **b** Pattern from a grain in the outer layer, indexed as  $\alpha$ -Al<sub>2</sub>O<sub>3</sub>, with zone axis [220 $\bar{1}$ ]. **c** Pattern from a grain in the inner layer, indexed as  $\alpha$ -Al<sub>2</sub>O<sub>3</sub>, with zone axis [32 $\bar{1}$ 1]

inner layer which consisted of  $\alpha$ -Al<sub>2</sub>O<sub>3</sub>. Representative CBED patterns are presented in Fig. 8. The positions of the oxide grains are circled in Fig. 7a. The zone axes for the patterns are [01 $\bar{1}$ ], [220 $\bar{1}$ ] and [32 $\bar{1}$ 1]. In a recent paper we reported a similar two-layered structure of the base oxide formed on the alloy Kanthal AF at 900 °C [27, 29].

#### TEM Investigation After 168 h in O<sub>2</sub> + 40% H<sub>2</sub>O

Figure 9a shows an overview of the FIB/SEM-prepared TEM cross-section window for a sample that was exposed for 168 h in wet O<sub>2</sub>. At this stage, the well-separated nodules of thick oxide present on the 24 h sample (Figs. 3a, 4a) have merged, forming a ring-shaped region of thick oxide around the Y-rich RE particle. Similarly to the 24 h sample, the thick oxide patch has a two-layered structure (Fig. 9b). The continuous inner oxide layer now has a varying thickness. It is thinnest, ~160 nm, at the location where the oxide ring is thickest. The inner oxide becomes gradually thicker when approaching the base oxide or the Y-rich particle. The morphologies of the oxide grains are similar to those on the 24 h sample. Thus, the grains in the inner layer are equiaxed while the oxide grains in the outer layer are elongated and contain dark stripes (corresponding to planar faults). As noted above, these morphologies are characteristic of  $\gamma$ -alumina (in the outer layer) and  $\alpha$ -alumina (in the inner layer), respectively. Again, some voids were observed close to the interface between the inner and outer layer.

STEM/EDX mapping (Fig. 10) shows that the particle contains mainly Y with some Ti, Zr and Si. Interestingly, some Si is found in the alumina scale directly above the particle, the Al/Si ratio being about 6:1. The chemical composition of the oxidized RE particle varies. A typical composition for the Y-rich area is (out of cations): Y 50 at.%, Zr 5 at.%, Ti <5 at.%, with the remainder being mainly Fe, Cr, and Al. This particle is also separated from the alloy by an Al<sub>2</sub>O<sub>3</sub> layer.

In order to further analyze the region with the particle, scatter plots were obtained from the EDX maps. In the plots, regions with different compositions were first selected. Then colours were assigned to represent each selected composition region and the result is displayed in the EDX phase map in Fig. 10b, which shows the

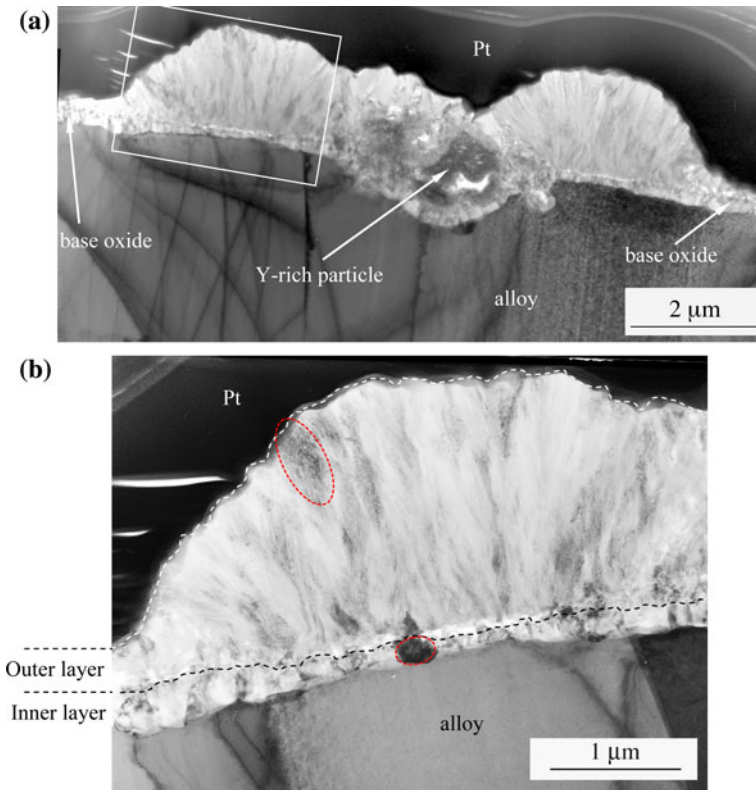


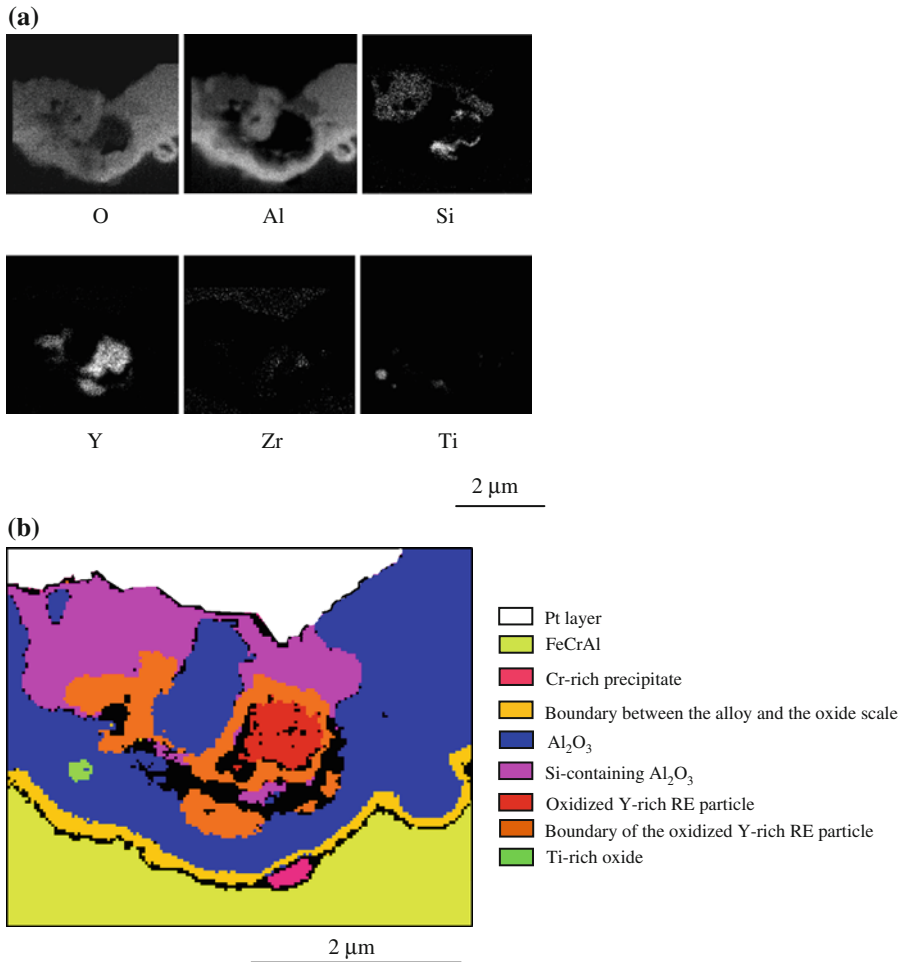
**Fig. 9** **a** TEM bright field cross-section image of the oxide scale formed on the sample exposed to  $O_2$  with 40%  $H_2O$  for 168 h (See Fig. 3c). Close to the Y-rich particle the oxide scale is much thicker than the base oxide. **b** Enlarged image of the marked area in (a), showing a two-layered structure. Diffraction patterns of the circled grains are presented in Fig. 11

complex scale microstructure. The regions indicated in the figure are attributed to the FeCrAl alloy, a Cr-rich precipitate in the alloy, the boundary between the alloy and the oxide scale, the oxidized Y-rich particle, which contains some Si and Ti, the boundary of the RE particle, the alumina scale, the Si-containing alumina scale and the protective Pt layer.

TEM diffraction studies confirmed the indication from TEM bright field imaging (Fig. 9), proving that the outer layer consists of  $\gamma-Al_2O_3$ , while the inner layer is  $\alpha-Al_2O_3$ . Selected area electron diffraction (SAED) patterns illustrating this are shown in Fig. 11a, b. The positions of corresponding oxide grains are circled in Fig. 9b. They are indexed as with zone axis  $[001]$  and  $[1\bar{1}00]$ , respectively.

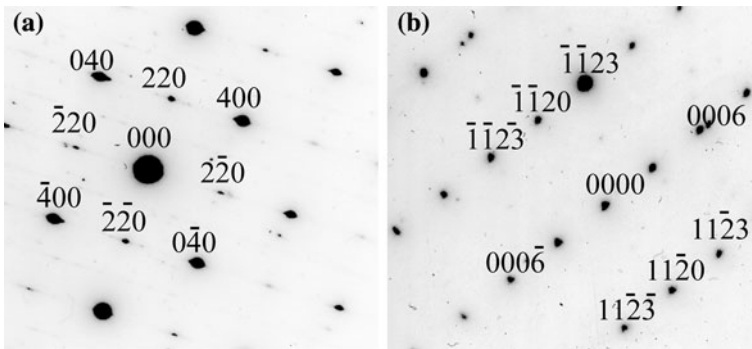
#### TEM Investigation After 168 h in Dry $O_2$

Figure 12a displays a TEM bright field cross-section image of the thick oxide patch formed after 168 h in dry oxygen. Similarly to the sample exposed for 24 h in the same atmosphere, the patch of thick oxide has a rough surface. A continuous row of



**Fig. 10** **a** STEM bright field image and STEM/EDX maps of the Y-rich RE particle (168 h, O<sub>2</sub> with 40% H<sub>2</sub>O, compare Fig. 9a). In addition to Y, the particle contains some Zr and Ti as well. Si is found in the outer part of the oxide scale as well as in the particle. A continuous alumina layer separates the particle from the alloy substrate. **b** Phase map for the region containing the Y-rich RE particle

small ( $\sim 80$  nm) equiaxed oxide grains in the inner layer is distinguishable. Interestingly, the morphology of the oxide grains in the outer layer has changed significantly compared to 24 h. There are two types of oxide grains with markedly different morphology. Just above the inner oxide layer there are many large equiaxed grains, forming a continuous region of varying thickness. These oxide grains are more than 100 nm in size, sometimes with intergranular or intragranular voids and are always free of dark stripes. At the gas/oxide interface there are many elongated oxide grains, with dark stripes (planar defects), like those observed on the 24 h sample. The characteristic morphologies allows us to conclude that the upper part of the alumina scale consists of two phases,  $\gamma$ -alumina at the scale/gas interface



**Fig. 11** SAED patterns from the circled oxide grains in the thick oxide patch (168 h,  $\text{O}_2$  with 40%  $\text{H}_2\text{O}$ ). **a** Diffraction pattern from a grain in the outer layer, indexed as  $\gamma$ - $\text{Al}_2\text{O}_3$ , with zone axis  $[001]$ . **b** Pattern from a grain in the inner layer, which has been indexed as  $\alpha$ - $\text{Al}_2\text{O}_3$ , with zone axis  $[110]$

and  $\alpha$ -alumina in the vicinity of the Cr enriched region that corresponds to the original sample surface. Again this was verified by electron diffraction shown below. Intergranular voids are found at the interface between the two types of grains in the outer oxide. In contrast, the number of voids at the interface between the inner and outer oxide layer has decreased compared to the situation after 24 h. Similarly to the corresponding 24 h exposure, regions with different chemical composition can be distinguished in the STEM/EDX linescan (Fig. 12b) across the oxide scale, confirming its two-layered structure with a Cr-rich band in between. Linescans across the entire scale show little variation in the concentrations of Fe, Cr and Al in the outer oxide (region III), which is basically pure alumina. In parts of the outer alumina layer Mg was detected, reaching up to 4 at. %.

The outermost elongated grains were identified as  $\gamma$ - $\text{Al}_2\text{O}_3$ , while the equiaxed grains in the inner part of the outer layer, as well as all grains in the thin inner layer, consist of  $\alpha$ - $\text{Al}_2\text{O}_3$ . This is shown in the CBED patterns presented in Fig. 13. The zone axis for the patterns are  $[001]$ ,  $[2\bar{1}\bar{1}0]$  and  $[1\bar{1}00]$ .

## Discussion

When the FeCrAl alloy Kanthal AF is exposed to dry or wet  $\text{O}_2$  at 900 °C, three characteristic scale features develop: a thin base oxide covering most of the surface, oxidized RE particles, and patches of relatively thick alumina scale associated with the Y-rich RE particles [28]. It was shown previously that the base oxide has developed a duplex structure already after one hour, consisting of a continuous inward growing  $\alpha$ - $\text{Al}_2\text{O}_3$  layer at the bottom and an outward growing  $\gamma$ - $\text{Al}_2\text{O}_3$  layer on top [29]. In dry  $\text{O}_2$ , the outer  $\gamma$ - $\text{Al}_2\text{O}_3$  layer gradually transformed to a mixture of  $\alpha$ - $\text{Al}_2\text{O}_3$  and spinel ( $\text{Mg}_{1-x}\text{Fe}_x\text{Al}_2\text{O}_4$ ):



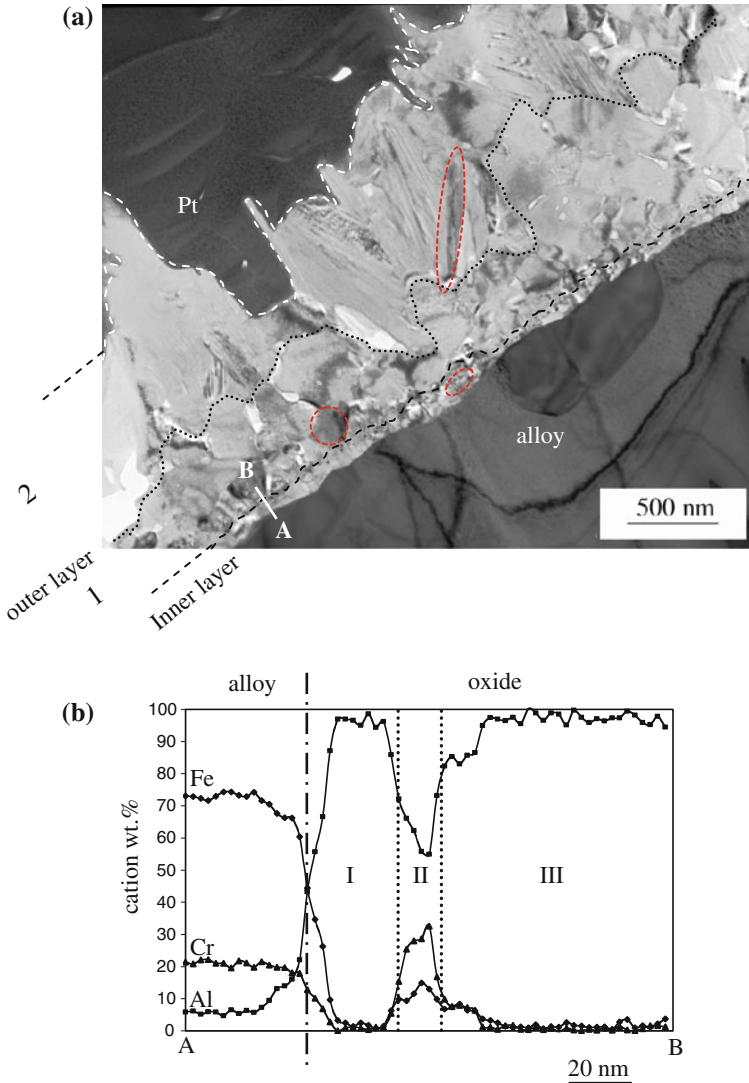
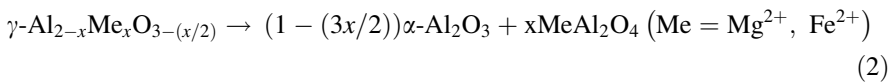


**Fig. 12** **a** TEM bright field cross-section image of the thick oxide patch formed close to an Y-rich particle on the sample exposed to  $O_2$  for 168 h (See Fig. 3d). The line AB indicates the position where the linescan was acquired. **b** STEM/EDX linescan across the thick oxide scale (168 h, dry  $O_2$ ). The three regions in the EDX linescan profile indicates a layered structure. Diffraction patterns of the circled grains are presented in Fig. 13



In contrast, transformation of  $\gamma\text{-Al}_2\text{O}_3$  to  $\alpha\text{-Al}_2\text{O}_3$  was not observed in wet  $O_2$ , even after relatively long exposure times (168 h) [25, 27, 29, 34]. Previously it was shown that the RE oxide particles formed on Kanthal AF belong to different classes,

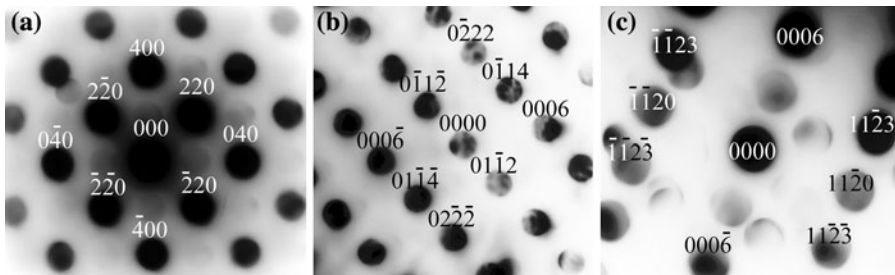


**Fig. 13** CBED patterns from *circled* oxide grains in the thick oxide patch (168 h, O<sub>2</sub>, Fig. 12). **a** Pattern from a grain in the outermost part of the outer layer, indexed as  $\gamma$ -Al<sub>2</sub>O<sub>3</sub>, with zone axis [001]. **b** Pattern from a grain in the inner part of the outer layer, indexed as  $\alpha$ -Al<sub>2</sub>O<sub>3</sub>, with zone axis [2̄1̄10]. **c** Pattern from a grain in the inner layer, indexed as  $\alpha$ -Al<sub>2</sub>O<sub>3</sub>, with zone axis [1100]

some being dominated by Y while others are dominated by Zr or Ti [26]. In addition to the RE elements, the oxide particles sometimes contain Si [23]. Micrometer-sized RE-rich intermetallic particles are reported to precipitate during processing because of the limited solubility of these elements in the alloy [15, 16]. When exposed to oxidizing environment at elevated temperature the RE-rich particles at the surface rapidly become fully oxidized. It is notable that the Y-rich RE particles strongly influenced the microstructure of the surrounding scale while the particles rich in Ti and Zr had no such effect. Thus, the oxidized Zr- and Ti-rich RE particles were surrounded by thin base oxide while the oxidized Y-rich RE particles were surrounded by patches of thicker alumina scale [26, 35]. The present study confirms the earlier reports on the effect of the RE rich particles on the oxide scale and reveals the detailed microstructure of the RE rich oxide particles and the adjacent alumina scale.

#### The Role of the Y-rich RE Particles

After 24 h oxidation in both dry and wet O<sub>2</sub>, the thick oxide patches have developed a two-layered structure similar to that of the base oxide. As in the case of the base oxide, it is argued that the Cr-rich band is a marker showing the original oxide/gas interface (see below). This implies that the  $\alpha$ -Al<sub>2</sub>O<sub>3</sub> (inner) layer grows mainly by inward oxygen diffusion while the  $\gamma$ -Al<sub>2</sub>O<sub>3</sub> (outer) layer grows mainly by outward cation diffusion. TEM shows that the thick oxide patches are 3–4 times thicker than the surrounding base oxide (see Table 2). In order to visualize the thickness ratios shown in Table 2, a plot displaying the thickness of the inner and outer layers for the base and thick oxide is presented in Fig. 14. The results show that the greater oxide thickness is due to the growth of the outer oxide layer, which is about 10 times thicker than in the surrounding base oxide. In contrast, the thick oxide patches feature an inner  $\alpha$ -Al<sub>2</sub>O<sub>3</sub> layer which is about 50% thinner compared to the surrounding base oxide. The relative thickness of the inner and outer layers in the thick oxide patches is influenced by water vapour. Thus, after 24 h the outer alumina layer is thicker in dry conditions than in wet O<sub>2</sub> (0.96 vs. 0.7) while the inner layer is thinner (0.04 vs. 0.1). In contrast, after 168 h both layers are thinner in

**Table 2** Measured scale thickness after 24 and 168 h exposure at 900 °C in dry O<sub>2</sub> and O<sub>2</sub> + H<sub>2</sub>O

Average thickness	Exposure condition					
	O <sub>2</sub>		O <sub>2</sub> + 40% H <sub>2</sub> O		O <sub>2</sub> + H <sub>2</sub> O	
	24 h		168 h		168 h	
	Thick oxide	Base oxide	Thick oxide	Base oxide	Thick oxide	Base oxide
Total	1	0.18	1.5	0.45	0.8	0.22
Inner layer	0.04 ± 0.03	0.06 ± 0.04	0.08 ± 0.04	0.30 ± 0.13	0.1 ± 0.04	0.16 ± 0.04
Outer layer	0.96 ± 0.32	0.12 ± 0.04	1.42 ± 0.36	0.15 ± 0.05	0.7 ± 0.20	0.06 ± 0.02
					1.9	0.6
					0.18 ± 0.04	0.4 ± 0.06
					1.72 ± 0.10	0.2 ± 0.04

The values refer to the thick oxide formed at the Y-rich particles and to the base oxide. Thickness values are given for both the inner and the outer part of the duplex scale. The values represent typical (average) values. For example the thick oxide may vary by a factor of 2 (see Fig. 9)



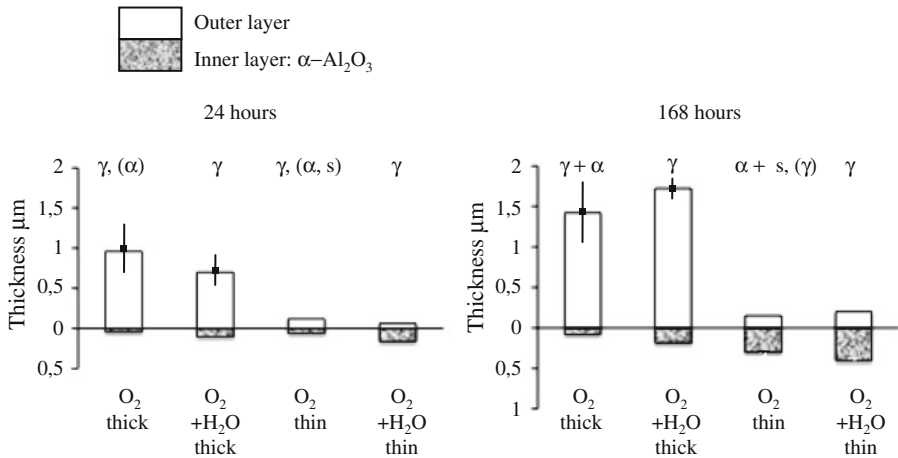


**Fig. 14** The figure summarizes the results on scale thickness and scale microstructure after 24 and 168 h exposure at 900 °C in dry O<sub>2</sub> and O<sub>2</sub> + H<sub>2</sub>O. The information is based on TEM measurements, see also Table 2. “Thick” and “thin” designate the thick oxide patches and the thin base oxide respectively. Note that in all cases, the inner oxide layer consists only of  $\alpha$ -Al<sub>2</sub>O<sub>3</sub>. The phase composition of the outer oxide layer is also indicated, “ $\alpha$ ” designating  $\alpha$ -Al<sub>2</sub>O<sub>3</sub>, “ $\gamma$ ”  $\gamma$ -Al<sub>2</sub>O<sub>3</sub>, and “s” spinel (MgAl<sub>2</sub>O<sub>4</sub>). Phases only present in small amounts are bracketed

dry O<sub>2</sub> (1.42 vs. 1.72) (0.08 vs. 0.18). This is mainly attributed to the partial transformation of  $\gamma$ -Al<sub>2</sub>O<sub>3</sub> in the outer layer to  $\alpha$ -Al<sub>2</sub>O<sub>3</sub> (see below).

Divalent cations, e.g. Fe<sup>2+</sup> and Mg<sup>2+</sup>, have appreciable solubility in  $\gamma$ -Al<sub>2</sub>O<sub>3</sub> [36]. Accordingly, it was reported that the outer,  $\gamma$ -alumina, part of the base oxide formed on Kanthal AF contained 10–30 at.% of Mg (cationic) [29]. The present study shows that Mg is also enriched in the outer  $\gamma$ -alumina layer of the thick oxide patches. However, the concentration of Mg only reaches 4 at.% (cationic). Because of the low concentration of Mg<sup>2+</sup> and Fe<sup>2+</sup> in  $\gamma$ -Al<sub>2</sub>O<sub>3</sub>, spinel formation according to reaction (2) does not occur, explaining the absence of spinel oxide (Mg<sub>1-x</sub>Fe<sub>x</sub>Al<sub>2</sub>O<sub>4</sub>) in the thick oxide patches. Otherwise, the phase composition of the thick oxide patches and the base oxide is the same.

It is interesting to speculate on why the Y-rich RE oxide particles are surrounded by thick oxide while the Y-poor RE oxide particles (dominated by Zr and Ti) have no apparent effect on the surrounding scale. Such a discussion must have the effect of “reactive elements” (RE) on the oxidation of alumina-forming alloys as a starting point. As noted in the introduction, the corpus of work on this subject is very large. It must first be emphasized that investigations of the RE effect on alumina formers are typically carried out at considerably higher temperature (1100–1300 °C) than in the present work. Also, the scale microstructures observed here are different from those described for FeCrAl(RE) alloys after oxidation at higher temperature. One example is the transient aluminas that play a prominent role at 900 °C while they are of less importance at 1200–1300 °C. Nevertheless, it is considered that the theories proposed for the RE effect in the literature are relevant to this study.

It may be noted that the thicker oxide patches around the Y-rich oxide particles have similar radius (3–6  $\mu\text{m}$ ) (see Figs. 2, 3) and that while the oxide patches grow thicker with time, they do not spread out over the surface. The roughly radial distribution of thick oxide around the Y-rich oxide particles implies that the faster oxidation is caused either by the Y-rich oxide particle itself or by compositional gradients in the alloy around the particle. To argue the first case one may surmise that the Y-rich oxide particles have some catalytical property that somehow influences the growth of the surrounding alumina scale. Indeed, yttrium oxide has been reported to be a catalyst for oxygen reduction [37]. However, it is considered improbable that oxygen reduction on the scale surface is rate limiting for scale growth in the present case, except perhaps during heat-up, in the very beginning of the exposure.

Commercial FeCrAl(RE) alloys typically contain RE-rich precipitates formed at high temperature during manufacturing. In these precipitates the REs are associated with p-block elements, primarily oxygen, carbon, nitrogen, silicon and sulphur, often forming mixtures [38, 39]. Hence the precipitates may be described as partly oxidized carbides, nitrides etc. The observation of silicon in one of the oxidized Y-rich particles (see Fig. 10) implies that it originally contained yttrium silicide. It is considered that the RE-rich oxide particles observed in the present study have formed by oxidation of RE-rich precipitates. This implies that the two classes of RE-rich oxide particles observed in this study correspond to Y-rich and Zr + Ti-rich particles, respectively, present in the alloy. It is suggested that the rapid oxidation of the alloy in the vicinity of the Y-rich oxide particles is caused by concentration gradients in the alloy that have developed around the Y-rich particles during alloy processing.

As temperature decreases during processing, the RE-rich particles grow, resulting in a corresponding depletion of REs in the surrounding alloy matrix. Hence, although evidence for such compositional gradients is lacking, it is argued that the alloy close to the Y-rich precipitates is depleted in yttrium. It may be noted that Y gradients in the alloy cannot be detected using EDX in microprobe, TEM or SEM, because the solubility of Y is far below the detection limit (about 0.1 wt.%). Due to the relatively low exposure temperature, it is expected that the concentration gradients remain during exposure. Using the relation between diffusion length ( $x$ ) and diffusion coefficient ( $D$ )  $x = (Dt)^{1/2}$ , and putting  $t = 24$  h, puts an upper boundary on the diffusion coefficient of Y in the alloy of  $5 \times 10^{-13} \text{ cm}^2 \text{ s}^{-1}$ . Similar concentration gradients are expected to exist around the Zr and Ti-rich particles. Hence, if the thick oxide is related to these gradients in the alloy, the effect of yttrium on oxide growth must be different from that of Zr and Ti.

There is ample evidence in the literature that the presence of Y in the alloy decreases the rate of outward growth of alumina scales [3, 5, 40]. Hence, the ratio between the inward diffusion of oxygen ions and the outward diffusion of cations in alumina scales on FeCrAl alloys is reported to increase with the addition of Y [41]. Although the detailed mechanism is not known, most workers believe that Y influences grain boundary transport through the alumina scale,  $\text{Y}^{3+}$  ions being reported to be enriched in the oxide grain boundaries [42]. Working with a number of FeCrAl alloys in the temperature range 1100–1300 °C, Nychka and Clarke [41]

report on the formation of a duplex scale structure, which resembles that observed in the present case. Thus, they observe an outer  $\alpha$ -alumina layer with equiaxed grains and an inner  $\alpha$ -alumina layer with columnar grains. The authors consider that the two layers correspond to outward- and inward- growing alumina, respectively. It is suggested that the microstructure of the scale observed in the present work corresponds to that reported in Ref. [41]. Hence, it is considered that the top layer of the scales observed in the present study, consisting of  $\gamma$ -alumina in  $O_2 + H_2O$  environment and of a mixture of equiaxed  $\alpha$ -alumina and  $\gamma$ -alumina in dry  $O_2$ , have formed by outward growth. Thus, it is argued that the thick oxide patches observed around the Y rich oxide agglomerates are due to a local depletion of the alloy in Y, the low Y concentration explaining the tendency for enhanced outward growth of the alumina scale. In this scenario then, the tendency to form a thick layer of transient alumina on top of a thin inner  $\alpha$ -alumina layer and a thin transient alumina layer on top of a relatively thick bottom  $\alpha$ -alumina (see Fig. 14; Table 2) reflects the relative importance of outward and inward oxide growth which, in turn, is mainly governed by the concentration of Y in the alloy substrate.

It is notable that the transient alumina layer making up the top, outward growing, scale layer does not cease to grow once a continuous  $\alpha$ -alumina layer has formed underneath. On the contrary, the outer metastable alumina layer continues to grow in thickness throughout the exposure (See e.g., Fig. 14). The outward growth of the transient alumina layer of course implies a corresponding flux of cations through the inner  $\alpha$ -alumina layer. It is well known that  $\alpha$ -alumina is able to transport cations (see above). However, the present observations also imply that upon leaving the inner  $\alpha$ -alumina part of the scale, the cations ( $Al^{3+}$  with some  $Mg^{2+}$ ) enter the outer scale layer to form metastable alumina on its surface. This may appear surprising in view of the fact that the transformation of  $\alpha$ -alumina to metastable alumina is thermodynamically disallowed. This apparent paradox can be resolved by considering that the diffusion of ions through the  $\alpha$ -alumina layer is by grain boundary transport in the present case. Thus, the results suggest that the aluminium ions travelling through the  $\alpha$ -alumina layer via the grain boundaries have appreciably higher chemical potential than the aluminium ions in solid corundum.

It may be noted that chemical gradients in the alloy affecting other elements than Y may also play a role. Anyway, the lack of effect of the Zr and Ti rich oxide particles suggests that these elements have little effect on the mechanism of growth of the alumina scale.

The formation of a locally thick oxide is undesirable. Firstly, it may introduce high stresses which can lead to spallation [43]. Secondly, the Al reservoir of a FeCrAl alloy is limited, especially in foils. Hence, the formation of a thick and fast growing alumina is expected to shorten the lifetime of the alloy [44, 45].

### The Effect of Water Vapour

Recently, we reported that the presence of water vapour tends to stabilize  $\gamma$ - $Al_2O_3$  on Kanthal AF at 900 °C, preventing its transformation to  $\alpha$ - $Al_2O_3$  [25, 27, 29]. The present study shows the same effect in the case of the patches of thick oxide formed around the Y-rich particles. Thus, in  $O_2 + H_2O$  environment the top layer of the

duplex scale consists of only  $\gamma$ -Al<sub>2</sub>O<sub>3</sub> throughout the exposure (Fig. 9) while in dry O<sub>2</sub>,  $\gamma$ -Al<sub>2</sub>O<sub>3</sub> in the outer oxide layer gradually transforms into  $\alpha$ -Al<sub>2</sub>O<sub>3</sub>. The transformation has started after 24 h, and much of the outer oxide layer has transformed to  $\alpha$ -Al<sub>2</sub>O<sub>3</sub> after 168 h (see Figs. 7, 12a). Our results show that the phase transformation originates at the interface between the inner ( $\alpha$ -Al<sub>2</sub>O<sub>3</sub>) and outer ( $\gamma$ -Al<sub>2</sub>O<sub>3</sub>) layers (see Fig. 12a). It has been reported that the initiation of Al<sub>2</sub>O<sub>3</sub> phase transformations requires favourable nucleation sites [46], and in some instances a free surface [47]. In the present case, both favourable nucleation sites, i.e.  $\alpha$ -grains, and free surfaces, i.e., voids, are available at the interface.

The present study shows that the surface morphology of the thick oxide patches is influenced by water vapour (see Fig. 3). Thus, in dry O<sub>2</sub> (Figs. 7, 12) the top ( $\gamma$ -Al<sub>2</sub>O<sub>3</sub>) layer consists of relatively large blade-like crystallites forming a very uneven surface. In contrast, in O<sub>2</sub> + H<sub>2</sub>O environment the  $\gamma$ -Al<sub>2</sub>O<sub>3</sub> layer consists of somewhat smaller crystallites that assemble into a surface which is less rough (Figs. 4, 9). This effect of water vapour was not observed on the base oxide, which contains only a thin layer of  $\gamma$ -Al<sub>2</sub>O<sub>3</sub>.

## Conclusions

- The Y-rich RE oxide particles are surrounded by circular patches of thicker alumina scale. The corresponding particles enriched in Zr and Ti has no effect on alumina scale morphology. The oxidized Y-rich particles are totally surrounded by an alumina layer.
- The thick oxide patches surrounding the Y-rich RE particles exhibit a two-layered structure comprising a thick outward growing layer, originally consisting of  $\gamma$ -Al<sub>2</sub>O<sub>3</sub> and a thin, continuous inward growing  $\alpha$ -Al<sub>2</sub>O<sub>3</sub> layer. The  $\gamma$ -Al<sub>2</sub>O<sub>3</sub> layer continues to grow rather fast despite the presence of an inner  $\alpha$ -alumina layer.
- It is suggested that the formation of thick oxide patches around the Y-rich oxide particles, featuring enhanced outward growth of the alumina scale, is due to a local depletion of the alloy in Y.
- Water vapour stabilizes  $\gamma$ -Al<sub>2</sub>O<sub>3</sub> in the outer oxide scale and prevents the transformation to  $\alpha$ -Al<sub>2</sub>O<sub>3</sub>. In dry O<sub>2</sub> environment, the  $\gamma$ -Al<sub>2</sub>O<sub>3</sub> outer layer is transformed to  $\alpha$ -Al<sub>2</sub>O<sub>3</sub> with time. This process has already started after 24 h. The transformation originates immediately above the inner ( $\alpha$ -Al<sub>2</sub>O<sub>3</sub>) layer. In contrast, the  $\gamma$ -Al<sub>2</sub>O<sub>3</sub> has not transformed at all after 168 h in the humid environment.
- Water vapour affects the morphology of the thick oxide patches formed around the Y-rich RE particles. In dry environment, it has a blade-like shape, while the surface is less rough in humid environment.

**Acknowledgements** The authors are grateful to Bo Jönsson at Kanthal AB for discussions and advice throughout this work. This work was carried out within the Swedish High Temperature Corrosion Centre (HTC). It was supported by Kanthal AB and Sandvik Materials Technology AB and the National Graduate School in Materials Science at Chalmers University of Technology.

## References

1. R. Prescott and M. J. Graham, *Oxidation of Metals* **38**, 233 (1992).
2. P. Kofstad, *High-Temperature Corrosion*, Chap. 12 (Elsevier Applied Science, New York, 1988), p. 408.
3. D. P. Whittle and J. Stringer, *Philosophical Transactions of the Royal Society of London* **295**, 309 (1980).
4. R. Prescott, D. F. Mitchell, M. J. Graham, and J. Doychak, *Corrosion Science* **37**, 1341 (1995).
5. B. A. Pint, J. R. Martin, and L. W. Hobbs, *Oxidation of Metals* **39**, 167 (1993).
6. W. J. Quadakkers, W. Speier, H. Holzbrecher, and H. Nickel, in *Microscopy of Oxidation* (Cambridge, U.K., 1991), p. 149.
7. C. Mennicke, E. Schumann, J. L. Coze, J. L. Smialek, G. H. Meier, and M. Ruhle, in *The Third International Conference Of Microscopy Of Oxidation*, eds. S. B. Newcomb and J. A. Little (The Institute of Materials, University of Cambridge, 1996) p. 95.
8. J. L. Smialek, D. T. Jayne, and J. C. Schaeffer, *Thin Solid Films* **253**, 285 (1994).
9. J. L. Smialek, *Metallurgical Transactions A-Physical Metallurgy and Materials Science* **22**, 739 (1991).
10. J. G. Smeggil, A. W. Funkenbusch, and N. S. Bornstein, *Metallurgical Transactions A-Physical Metallurgy and Materials Science* **17**, 923 (1986).
11. A. W. Funkenbusch, J. G. Smeggil, and N. S. Bornstein, *Metallurgical Transactions A-Physical Metallurgy and Materials Science* **16**, 1164 (1985).
12. K. M. Carling and E. A. Carter, *Acta Materialia* **55**, 2791 (2007).
13. Y. Jiang, J. R. Smith, and A. G. Evans, *Applied Physics Letters* **92**, Article Number: 141918 (2008).
14. H. Hindam and D. P. Whittle, *Journal of the Electrochemical Society* **129**, 1147 (1982).
15. I. M. Allam, D. P. Whittle, and J. Stringer, *Oxidation of Metals* **12**, 381 (1979).
16. I. M. Allam, D. P. Whittle, and J. Stringer, *Oxidation of Metals* **12**, 35 (1978).
17. P. Y. Hou, *Oxidation of Metals* **52**, 337 (1999).
18. B. A. Pint, *Oxidation of Metals* **48**, 303 (1997).
19. H. J. Grabke, G. Kurbotov, and H. J. Schmutzler, *Oxidation of Metals* **43**, 97 (1995).
20. A. B. Anderson, S. P. Mehandru, and J. L. Smialek, *Journal of the Electrochemical society* **132**, 1695 (1985).
21. J. Klöwer, *Materials and Corrosion* **51**, 373 (2000).
22. V. Kochubey, H. Al-Badairy, G. J. Tatlock, J. L. Coze, D. Naumenko, and W. J. Quadakkers, *Materials and Corrosion* **56**, 848 (2005).
23. H. Al-Badairy, G. J. Tatlock, S. Fawcett, P. Beahan, and J. Hunt, *Journal De Physique IV* **124**, 17 (2005).
24. E. Wessel, V. Kochubey, D. Naumenko, L. Niewolak, L. Singheiser, and W. J. Quadakkers, *Scripta Materialia* **51**, 987 (2004).
25. H. Götlind, F. Liu, J.-E. Svensson, M. Halvarsson, and L.-G. Johansson, *Oxidation of Metals* **67**, 251 (2007).
26. F. Liu, H. Josefsson, J.-E. Svensson, M. Halvarsson, and L.-G. Johansson, in *16th International Corrosion Congress* (Beijing China, 2005), p. 19.
27. F. Liu, H. Josefsson, J.-E. Svensson, M. Halvarsson, and L.-G. Johansson, *Materials at High Temperatures* **22**, 521 (2005).
28. H. Josefsson, F. Liu, J.-E. Svensson, M. Halvarsson, and L.-G. Johansson, in *Electrochemical Society, 206th Joint International Meeting, Vol Proceeding Volume on High Temperature Corrosion and Materials Chemistry* (Honolulu, 2005).
29. F. Liu, H. Götlind, J.-E. Svensson, M. Halvarsson, and L.-G. Johansson, *Corrosion Science* **50**, 2272 (2008).
30. H. Josefsson, F. Liu, J.-E. Svensson, M. Halvarsson, and L.-G. Johansson, *Materials and Corrosion* **56**, 801 (2005).
31. F. Liu, J. E. Tang, T. Jonsson, S. Canovic, K. Segerdal, J.-E. Svensson, and M. Halvarsson, *Oxidation of Metals* **66**, 295 (2006).
32. J. Doychak, J. L. Smialek, and T. E. Mitchell, *Metallurgical Transactions A* **20A**, 499 (1989).
33. A. Larsson and S. Ruppi, *International Journal of Refractory Metals & Hard Materials* **19**, 515 (2001).

34. J. Engkvist, S. Canovic, F. Liu, H. Götlind, J.-E. Svensson, L.-G. Johansson, M. Olsson, and M. Halvarsson, *Materials at High Temperatures* **26**, 199 (2009).
35. S. Canovic, J. Engkvist, F. Liu, H. Götlind, K. Hellström, J.-E. Svensson, L.-G. Johansson, M. Olsson, and M. Halvarsson, *Journal of Electrochemistry Society* submitted (2009).
36. M. Kusunoki, M. Rokkaku, and Y. Ikuhara, *Materials Transactions JIM* **39**, 110 (1998).
37. B. Tveten, G. Hultquist, and D. Wallinder, *Oxidation of Metals* **55**, 279 (2001).
38. D. R. Sigler, *Oxidation of Metals* **32**, 337 (1989).
39. B. G. Mendis, K. J. T. Livi, and K. J. Hemker, *Scripta Materialia* **55**, 589 (2006).
40. D. Naumenko, V. Kochubey, L. Niewolak, A. Dymiati, J. Mayer, L. Singheiser, and W. J. Quadackers, *Journal of Material Science* **43**, 4550 (2008).
41. J. A. Nychka and D. R. Clarke, *Oxidation of Metals* **63**, 325 (2005).
42. W. J. Quadackers, J. Jedlinski, K. Schmidt, M. Krasovec, and G. Borchardt, *Applied Surface Science* **47**, 261 (1991).
43. J. D. Kuenzly and D. L. Douglass, *Oxidation of Metals* **8**, 139 (1974).
44. J. R. Nicholls, R. Newton, M. J. Bennett, H. E. Evans, H. Al-Badairy, G. J. Tatlock, D. Naumenko, W. J. Quadackers, G. Strehl, and G. Borchardt, in *EFC Workshop*, Vol. 34 (European Federation of Corrosion Publications, Frankfurt/Main, 2001).
45. R. Newton, M. J. Bennett, J. P. Wilber, J. R. Nicholls, D. Naumenko, W. J. Quadackers, H. Al-Badairy, G. Tatlock, G. Strehl, G. Borchardt, A. Telieps, B. Jönsson, A. Westerlund, V. Guttman, M. Maier, and P. Beaven, in *EFC Workshop*, Vol. 34 (European Federation of Corrosion Publications, Frankfurt/Main, 2001), p. 15.
46. J. C. Yang, E. Schumann, I. Levin, and M. Ruhle, *Acta Materialia* **46**, 2195 (1998).
47. N. Lindulf, M. Halvarsson, H. Nordén, and S. Vuorinen, *Thin Solid Films* **253**, 311 (1994).